American Journal of Energy Engineering
2026, Vol. 14, No. 3, pp. 158–171
https://doi.org/10.11648/j.ajee.20261403.17

SciencePG
Science Publishing Group

Research Article

Absorber-Doping Electrical Trade-off and MgF_2 Optical Enhancement in CIGS/In_2S_3 Thin-Film Solar Cells: A TCAD Analysis

Moussa Toure[1], Sidi Mohamed Mohamed-Yahya[2], Cheick Tidiane Goudiaby[1], Ahmed Mohamed-Yahya[2], Mamadou Lamine Samb[1, *]

[1]Department of Physics and Chemistry, Iba Der Thiam University, Thies, Senegal

[2]Applied Research Unit for Renewable Energies, University of Nouakchott, Nouakchott, Mauritania

Abstract

Thin-film Cu(In,Ga)Se2 (CIGS) solar cells with a non-toxic In_2S_3 buffer are a credible alternative to CdS-based devices. This work investigates an Al-Ni/MgF_2/ZnO:Al/i-ZnO/In_2S_3/CIGS/Mo solar-cell architecture using Silvaco ATLAS, with particular emphasis on the influence of CIGS absorber acceptor concentration (N_A, 1×10^{14}–1×10^{17} cm^{-3}) on J_{sc}, V_{oc}, FF, η, and the apparent series (R_s) and shunt (R_{sh}) resistances, with and without an MgF_2 antireflection coating. V_{oc} rises almost monotonically with N_A (+32%) while J_{sc} falls (−6.6%), so the pronounced non-monotonic evolution of FF primarily determines the location of the efficiency maximum. The highest simulated efficiency occurs at $N_A = 3\times10^{16}$ cm^{-3} (η = 23.65% with MgF_2 versus 20.99% without), but this maximum sits inside a fairly flat doping window (1×10^{16}-6×10^{16} cm^{-3}, η ≥ 95% of the peak) rather than a single sharp optimum. The resulting data reveal a strong association between the FF collapse and the increase in apparent R_s ($r \approx -0.99$ overall, ≈ -0.999 above 3×10^{16} cm^{-3}), linking the efficiency roll-off to degraded resistive transport without proving a single cause. The MgF_2 layer delivers a nearly constant J_{sc} gain (12.16%), a marginal V_{oc} effect (0.4-0.5%), and a negligible FF effect, so its efficiency gain (12.3-12.8%) is almost entirely inherited from J_{sc}. Together, these results distinguish the electrical trade-off associated with absorber doping from the predominantly optical contribution of MgF_2 and provide a practical doping window for CIGS/In_2S_3 device design.

Keywords

CIGS, In_2S_3, MgF_2 Antireflection Coating, Apparent Series Resistance, Apparent Shunt Resistance, Doping Window, Silvaco ATLAS, Thin-Film Solar Cell

1. Introduction

The accelerating global deployment of renewable energy technologies has reinforced the need for photovoltaic devices combining high conversion efficiency, reduced material toxicity, and scalable thin-film processing. Within this context,

*Correspondence: Mamadou Lamine Samb (mlsamb@univ-thies.sn)

Received: 22 August 2026; **Accepted:** 1 September 2026; **Published:** 20 September 2026

CIGS-based technologies remain particularly attractive because their absorber properties and heterojunction architecture can be engineered over a broad range. Thin-film CIGS solar cells remain among the most promising photovoltaic technologies, with a certified record efficiency of 23.35% [1], further demonstrating the potential of heavy-alkali post-deposition treatments [2], while non-toxic flexible architectures have recently reached efficiencies of 17.81% [3]. These advances are consistent with the most recent reference efficiency tables [4, 5]. Indium sulfide (In_2S_3) has emerged as a promising non-toxic alternative to the conventional CdS buffer layer [6], with certified efficiencies exceeding 16% [7] and photovoltaic performance comparable to that of CdS-based devices [8, 9]. However, recent atomic-scale investigations indicate that the In_2S_3/CIGS interface is chemically more complex than that represented by an idealized band alignment [10], underscoring the broader importance of band-alignment and interface-related effects when assessing the electrical behavior of CIGS-based heterojunctions [11].

The photovoltaic performance of CIGS/In_2S_3 solar cells is strongly influenced by the acceptor doping concentration of the CIGS absorber (N_A), which affects the main photovoltaic parameters, including the short-circuit current density (Jsc), open-circuit voltage (Voc), fill factor (FF), and conversion efficiency (η) [8, 9, 12, 13]. Although the influence of absorber doping on these parameters has been extensively investigated, the relationship between doping-induced variations in device performance and the corresponding parasitic resistive effects remains comparatively less explored. In particular, the series resistance (Rs) and shunt resistance (Rsh), which can be derived from the local characteristics of the J-V curve [14], provide useful complementary indicators for interpreting changes in the fill factor and overall device performance, as recently illustrated for CIGS/In_2S_3 heterojunctions [15].

In addition to the electrical properties governed by the absorber and buffer layers, optical losses at the front surface constitute another important factor limiting the performance of thin-film solar cells. The incorporation of an MgF_2 antireflection layer can reduce front-surface reflection and thereby enhance the photocurrent reaching the absorber. Its contribution can consequently be distinguished from the electrical effects associated with variations in absorber doping, providing a useful framework for assessing the combined electrical and optical behavior of the device.

Accordingly, this study investigates the influence of CIGS acceptor doping concentration on the photovoltaic and resistive characteristics of CIGS/In_2S_3 solar cells, with particular emphasis on the evolution of Jsc, Voc, FF, η, Rs, and Rsh. The analysis also examines the effect of an MgF_2 antireflection layer on device performance in order to distinguish optical gains from doping-related electrical effects. Particular attention is given to the existence of a favorable doping range rather than to a single optimum value, to the pronounced degradation of the fill factor at high doping concentrations, and to the relationship between this degradation and the evolution of the parasitic resistances. This combined analysis provides a more comprehensive interpretation of the electrical and optical factors governing the performance of CIGS/In_2S_3 solar cells.

2. Materials and Methods

2.1. Simulated Structure

Simulations were carried out with the Silvaco ATLAS/DeckBuild solver [16], which self-consistently solves Poisson's equation, the electron/hole continuity equations, and the drift-diffusion transport equations [17, 18]:

$$\nabla \cdot (\varepsilon \nabla \psi) = -q\,(p - n + N_D^+ - N_A^-) \quad (1)$$

$$\frac{\partial n}{\partial t} = \frac{1}{q}\nabla \cdot \vec{J}_n + G_n - R_n \quad (2)$$

$$\frac{\partial p}{\partial t} = -\frac{1}{q}\nabla \cdot \vec{J}_p + G_p - R_p \quad (3)$$

$$\vec{J}_n = q\mu_n n\vec{E}_n + qD_n\nabla n \quad (4)$$

$$\vec{J}_p = q\mu_p p\vec{E}_p - qD_p\nabla p \quad (5)$$

$$D_{n,p} = \frac{\mu_{n,p}k_BT}{q} \quad (6)$$

where ψ is the electrostatic potential, ε the local permittivity, q the elementary charge, n and p the electron and hole concentrations, N_D^+ and N_A^- the ionized donor and acceptor densities, J_n and J_p the electron and hole current densities, G and R the generation and recombination rates (including Shockley-Read-Hall), and D_n, D_p the diffusion coefficients related to the mobilities μ_n, μ_p through the Einstein relation. Both Shockley–Read–Hall (SRH) and Auger recombination were activated in the Silvaco ATLAS parameter set, using the simulator's default coefficients without additional CIGS-specific calibration. Two otherwise identical structures were simulated to isolate the effect of the antireflection coating: a full stack Aluminum/Nickel - MgF_2 - ZnO:Al - i-ZnO - In_2S_3 - CIGS - Molybdenum, and a reference structure identical in every respect except for the removed MgF_2 layer (Table 1, Figure 1).

Table 1. *Layer stack and role of each layer in the simulated CIGS/In_2S_3/MgF_2 structure under Silvaco ATLAS.*

Layer	Role
Aluminum / Nickel	Front metal contact (grid)
MgF_2	Antireflection coating
ZnO:Al	Transparent conductive oxide (TCO)
i-ZnO	Intrinsic buffer layer
In_2S_3	Buffer layer (heterojunction with CIGS)
CIGS (Cu(In,Ga)Se2)	Main absorber
Molybdenum (Mo)	Back contact

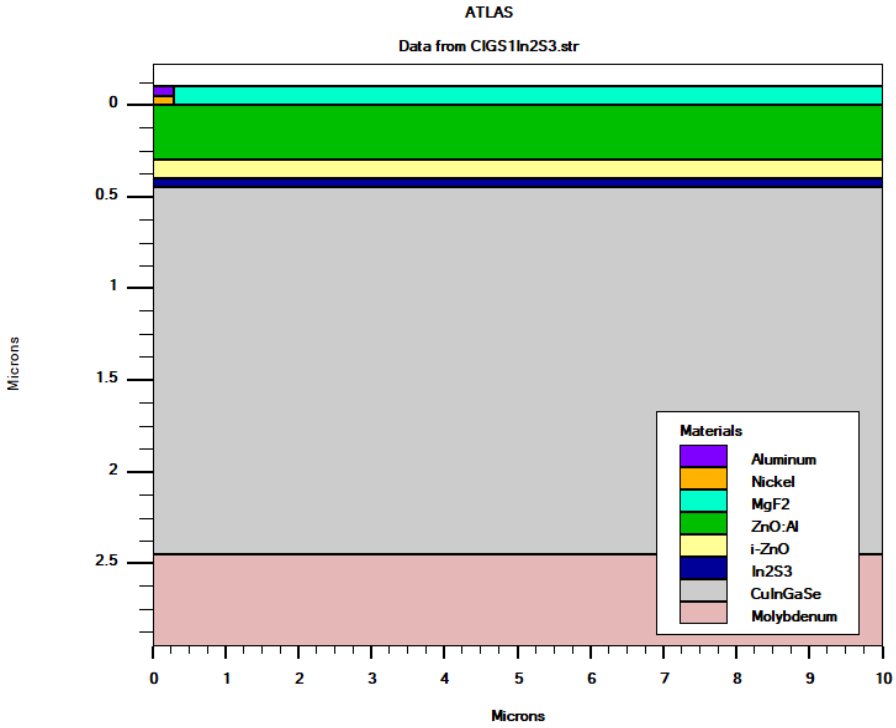

Figure 1. *Layer stack of the simulated CIGS/In_2S_3 structure under Silvaco ATLAS, including the MgF_2 antireflection layer.*

2.2. Band Diagram at the In_2S_3/CIGS Interface

The band diagram extracted at the In_2S_3/CIGS interface (Figure 2) shows a conduction-band "spike" alignment, with a discontinuity $\Delta Ec \approx +0.3$ eV, below the 0.4-0.5 eV critical threshold above which electron transport would be blocked [19, 20]. This moderate spike does not limit the transport of photogenerated carriers, which cross it by thermionic emission, and has the benefit of keeping minority carriers away from the region of highest interface defect density. Figure 2 therefore characterizes the reference heterojunction band alignment and is used here to establish the nature and magnitude of the conduction-band offset rather than to represent the doping-dependent evolution of band bending.

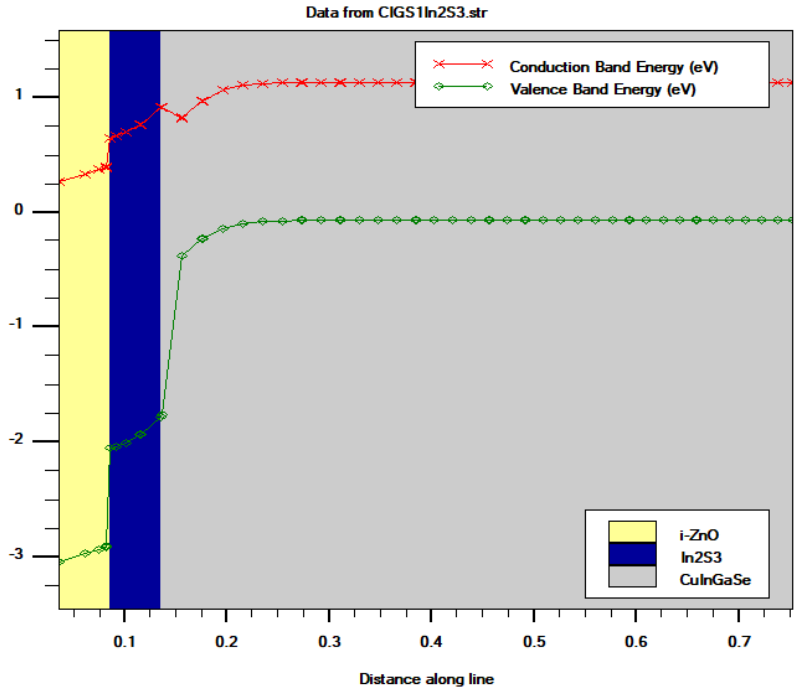

Figure 2. *Conduction- and valence-band diagram near the In_2S_3/CIGS heterojunction.*

2.3. Material Parameters

The physical parameters used for ZnO:Al, i-ZnO, In_2S_3, and CIGS are collected in Table 2, consistent with values reported for high-performance CIGS/In_2S_3 devices [15] and with the optical constants reported for thin-film CIGS [21]. For notational consistency, the optical gap is written Eg(300 K) rather than "Eg 300" as in the earlier table. The absorber gap, Eg(CIGS) = 1.2 eV, corresponds to a typical Ga/(In+Ga) ratio for the reference CIGS architectures used in this work; it is kept fixed (no gallium grading) throughout the doping sweep, which is likewise noted as a limitation in Section 3.10.

The swept parameter is the acceptor concentration N_A of the CIGS absorber, from 1×10^{14} to 1×10^{17} cm^{-3} (Table 2, "Acceptor concentration N_A" row), with every other quantity in Table 2 held constant.

Table 2. *Physical parameters used in the ATLAS simulation for the ZnO:Al, i-ZnO, In_2S_3, and CIGS layers (corrected notation: Eg(300 K), N_C(300 K), N_V(300 K)).*

Parameter	ZnO:Al	i-ZnO	In_2S_3	CIGS
Optical gap Eg(300 K) (eV)	3.3	3.3	2.7	1.2
Electron affinity χ (eV)	4.45	4.45	4.2	4.5
Relative dielectric permittivity εr	9	9	13.5	13.6
Thickness d (μm)	0.3	0.1	0.05	2
Effective electron DOS N_C(300 K) (cm^{-3})	2.2×10^{18}	2.2×10^{18}	2×10^{19}	2.2×10^{18}
Effective hole DOS N_V(300 K) (cm^{-3})	1.8×10^{19}	1.8×10^{19}	2×10^{17}	1.8×10^{19}
Donor concentration N_D (cm^{-3})	10^{20}	10^{14}	10^{17}	—
Acceptor concentration N_A (cm^{-3})	—	—	—	Variable (1×10^{14}-1×10^{17})
Electron mobility μ_n ($cm^2.V^{-1}.s^{-1}$)	100	100	50	100
Hole mobility μ_p ($cm^2.V^{-1}.s^{-1}$)	25	25	15	25
Electron lifetime τ_n (s)	10-10	10-10	10-9	10-7

Parameter	ZnO:Al	i-ZnO	In_2S_3	CIGS
Hole lifetime τ_p (s)	10-10	10-10	10-9	10-7
Interface defect density Dit ($cm^{-2}.eV-1$)	—	—	8×10^{11}	—

2.4. Simulation Conditions and Extracted Quantities

Current-voltage (J-V) characteristics are simulated under standard AM1.5G illumination (100 mW cm^{-2}) at 300 K. The extracted photovoltaic quantities (Jsc, Voc, FF, η) follow the usual single-diode definitions [14]:

$$FF = \frac{V_{mpp}\, J_{mpp}}{V_{oc}\, J_{sc}} \tag{7}$$

$$\eta = \frac{P_{max}}{P_{in}} = \frac{FF \cdot J_{sc} \cdot V_{oc}}{P_{in}} \tag{8}$$

The parasitic resistances are extracted from the local slope of the J-V curve:

$$R_s = -\left.\frac{dV}{dJ}\right|_{V \approx V_{oc}} \tag{9}$$

$$R_{sh} = -\left.\frac{dV}{dJ}\right|_{J \approx J_{sc}} \tag{10}$$

evaluated near Voc for Rs and near Jsc for Rsh. These two quantities do not necessarily correspond to an intrinsic series or shunt resistance in the sense of a single-diode equivalent circuit; for accuracy, they are referred to throughout the text as apparent series resistance and apparent shunt resistance, extracted from the simulated J-V curve using the local-slope method conventionally applied to thin-film cells [14].

3. Results and Discussion

3.1. J-V and P-V Characteristics at the Optimal Doping Level

The J-V and P-V characteristics obtained at the doping level giving peak efficiency ($N_A = 3\times10^{16}$ cm^{-3}, justified in 3.5) are shown in Figures 3-4 for both configurations. The two J-V curves show an almost constant vertical offset across the whole voltage range, together with an identical open-circuit voltage and knee shape; on the P-V curve, the power peak occurs at the same voltage (V ≈ 0.69-0.70 V) in both cases, but its amplitude is about 12.6% higher with MgF_2, the signature of a predominantly optical, multiplicative effect on the photogenerated current within this model.

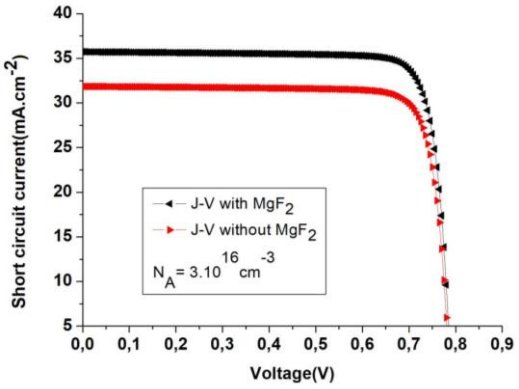

Figure 3. Compared J-V characteristics, with and without the MgF_2 antireflection layer ($N_A = 3\times10^{16}$ cm^{-3}).

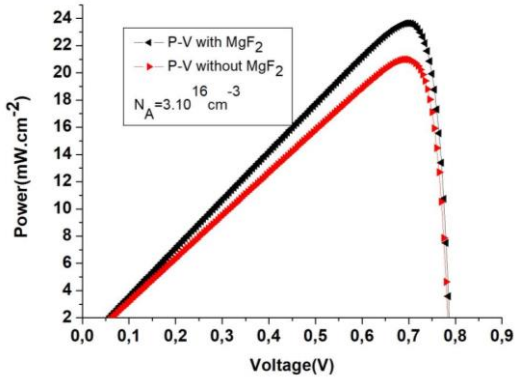

Figure 4. Compared P-V characteristics, with and without the MgF_2 antireflection layer ($N_A = 3\times10^{16}$ cm^{-3}).

3.2. Evolution of Jsc and Voc with Doping

Table 3. Evolution of Jsc with CIGS doping, with and without MgF_2.

Doping (cm^{-3})	Jsc with MgF_2 ($mA\ cm^{-2}$)	Jsc without MgF_2 ($mA\ cm^{-2}$)
1×10^{14}	37.3	33.2546
3×10^{14}	37.3215	33.2745
1×10^{15}	37.1304	33.1044
3×10^{15}	36.8001	32.8102
1×10^{16}	36.3226	32.3845
3×10^{16}	35.7256	31.8525
6×10^{16}	35.2724	31.4484
7×10^{16}	35.1682	31.3554
9×10^{16}	34.9996	31.2052
1×10^{17}	34.9231	31.137

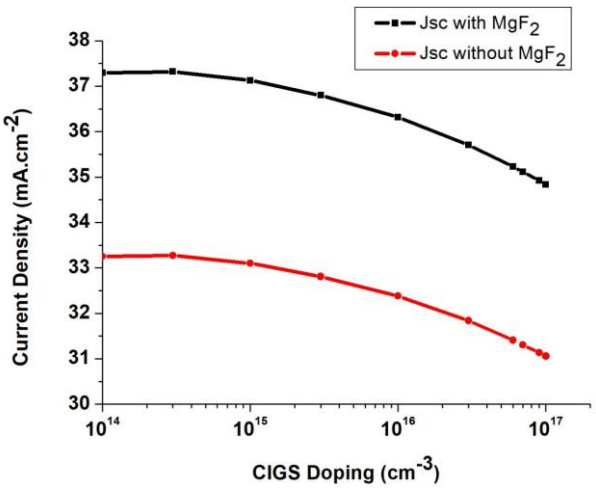

Figure 5. Jsc curves = f(N_A), with and without MgF_2.

Jsc falls monotonically by about 6.6% as N_A rises from 1×10^{14} to 1×10^{17} cm^{-3} (Table 3, Figure 5), for both configurations. This gradual decline is consistent with the narrowing of the space-charge region at high doping, which limits the collection of photogenerated carriers deeper in the absorber. Because the present model uses fixed carrier lifetimes across the N_A sweep (Table 2), lifetime-related mechanisms cannot be isolated from the present data, and the overall trend should be read as the net outcome of the modeled transport and collection effects rather than as evidence for a single dominant microscopic mechanism, consistent with other simulation-optimized CIGS/In_2S_3 architectures [8, 12]. Voc, by contrast, rises sharply and nearly linearly with the logarithm of the doping level (roughly +32% over the studied range, Table 4, Figure 6), consistent with the classic diode relation linking Voc to the Jsc/J_0 ratio [19, 20]. This opposite evolution of Jsc and Voc already signals that absorber doping produces competing effects; taken alone, however, neither parameter explains the sharp deterioration of the overall efficiency at high doping, which is why Section 3.3 turns to the fill factor as an additional diagnostic.

Table 4. Evolution of Voc with CIGS doping, with and without MgF_2.

Doping (cm^{-3})	Voc with MgF_2 (V)	Voc without MgF_2 (V)
1×10^{14}	0.625631	0.62223
3×10^{14}	0.660702	0.657483
1×10^{15}	0.696406	0.693307
3×10^{15}	0.727061	0.724032
1×10^{16}	0.75963	0.756503
3×10^{16}	0.788791	0.785754
6×10^{16}	0.807933	0.804943
7×10^{16}	0.812595	0.809543
9×10^{16}	0.821272	0.818065
1×10^{17}	0.825908	0.822668

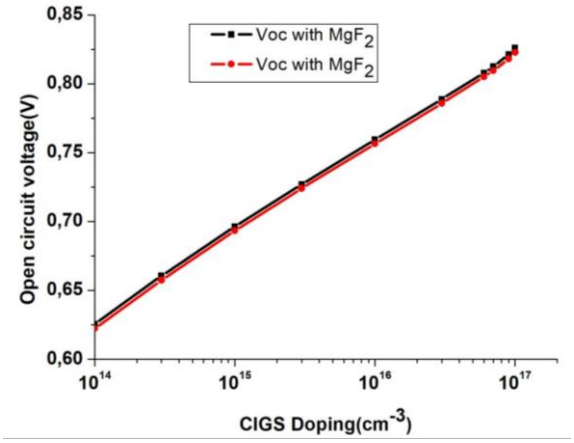

Figure 6. *Voc curves = f(N_A), with and without MgF_2.*

The relative gap between the two configurations remains remarkably stable for Jsc: 12.16% on average, with essentially zero spread across the ten sweep points (Table 9), confirming that, within this model, the antireflection layer acts in a strictly multiplicative way that is independent of the doping regime. Its effect on Voc is comparatively marginal (0.37 to 0.55%, Table 9), consistent with Voc's logarithmic dependence on Jsc.

3.3. Fill Factor and the Doping Window

Table 5. *Evolution of the fill factor FF with CIGS doping, with and without MgF_2.*

Doping (cm^{-3})	FF with MgF_2 (%)	FF without MgF_2 (%)
1×10^{14}	79.8178	79.781
3×10^{14}	81.3577	81.3204
1×10^{15}	82.3944	82.3449
3×10^{15}	82.9289	82.8696
1×10^{16}	83.3909	83.3353
3×10^{16}	83.9108	83.8825
6×10^{16}	81.0714	81.1636
7×10^{16}	78.0817	78.2353
9×10^{16}	69.5017	69.6948
1×10^{17}	64.6983	64.8738

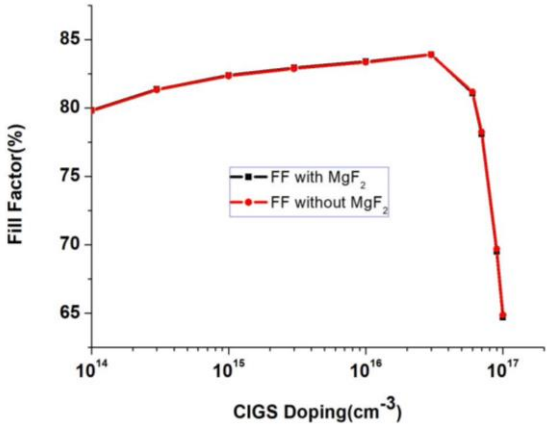

Figure 7. *FF curves = f(N_A), with and without MgF_2.*

Unlike Voc, whose monotonic rise contrasts with the eventual decline of the conversion efficiency, demonstrating that the open-circuit voltage alone cannot locate the optimum doping level, the fill factor exhibits a pronounced, non-monotonic optimum, making it the clearest indicator of the transition from a beneficial to a detrimental doping regime (Table 5, Figure 7). FF climbs from 79.8% to 83.9% between 1×10^{14} and 3×10^{16} cm^{-3}, indicating improved electrical performance, then drops sharply to 64.7% at 1×10^{17} cm^{-3}, identifying a transition between a transport-limited regime at low doping and a loss-dominated regime at high doping. Rather than reading this as a single sharp optimum, normalizing efficiency to its peak value (Figure 9, built from the Table 6 data) shows that efficiency stays at or above 95% of its maximum across a window $N_A \approx 1\times10^{16}$-$6\times10^{16}$ cm^{-3}, and above 90% over an even broader range. This window-based reading, rather than a point optimum, is more relevant for design purposes, since real-world doping inevitably has some spatial spread.

Table 6. *Evolution of the conversion efficiency η with CIGS doping, with and without MgF_2.*

Doping (cm^{-3})	EFF with MgF_2 (%)	EFF without MgF_2 (%)
1×10^{14}	18.6263	16.5083
3×10^{14}	20.0615	17.7908
1×10^{15}	21.3054	18.8994
3×10^{15}	22.1884	19.6862
1×10^{16}	23.009	20.4163

Doping (cm^{-3})	EFF with MgF_2 (%)	EFF without MgF_2 (%)
3×10^{16}	23.6461	20.9943
6×10^{16}	23.1035	20.5459
7×10^{16}	22.3138	19.8589
9×10^{16}	19.9777	17.7916
1×10^{17}	18.6611	16.6177

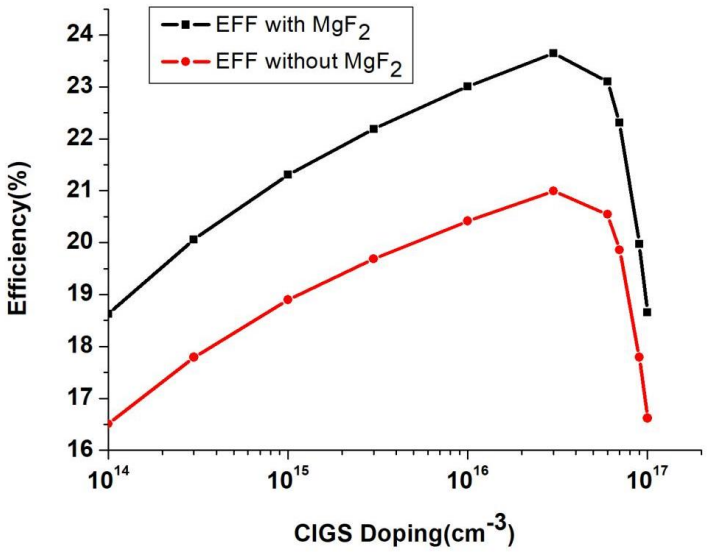

Figure 8. *η curves = f(NA), with and without MgF_2.*

Table 7. *Favorable doping window derived from the efficiency data reported in Table 6 (with MgF_2).*

N_A (cm^{-3})	η (%)	η / η_{max} (%)
1×10^{14}	18.63	78.8
3×10^{14}	20.06	84.8
1×10^{15}	21.31	90.1
3×10^{15}	22.19	93.8
1×10^{16}	23.01	97.3
3×10^{16} (max)	23.65	100.0
6×10^{16}	23.10	97.7
7×10^{16}	22.31	94.4
9×10^{16}	19.98	84.5
1×10^{17}	18.66	78.9

Window ≥ 95% of η_{max} (bold rows): $N_A \approx 1\times10^{16}$ to 6×10^{16} cm^{-3}.

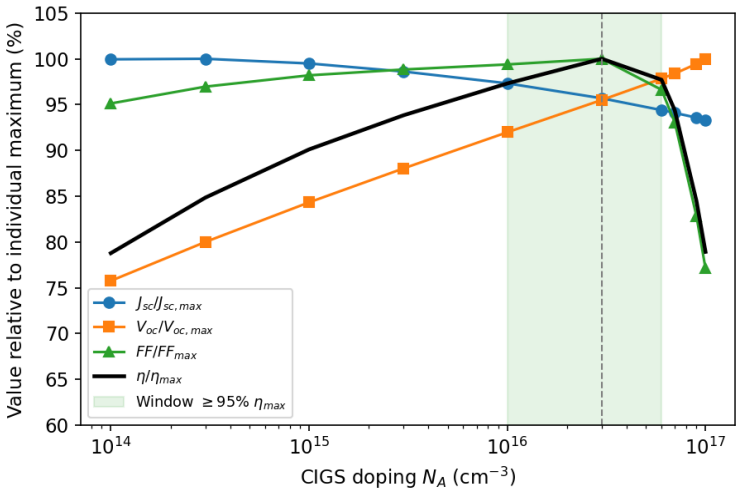

Figure 9. *Jsc-Voc-FF trade-off normalized to each quantity's individual maximum, showing the ≥95%-of-peak-efficiency doping window (with MgF_2).*

3.4. Apparent Parasitic Resistances and Their Correlation with the Fill Factor

Table 8. *Evolution of Rs and Rsh with CIGS doping, with and without MgF_2.*

Doping (cm^{-3})	Rs with MgF_2 ($\Omega \cdot cm^2$)	Rs without MgF_2 ($\Omega \cdot cm^2$)	Rsh with MgF_2 ($\Omega \cdot cm^2$)	Rsh without MgF_2 ($\Omega \cdot cm^2$)
1×10^{14}	0.984764	1.09949	3847.58	4257.25
3×10^{14}	0.913237	1.02116	4001.6	4446.64
1×10^{15}	0.875734	0.980682	2547.88	2867.72
3×10^{15}	0.869013	0.973678	2179.98	2424.33
1×10^{16}	0.875477	0.981051	1932.42	2179.98
3×10^{16}	0.901115	1.00809	2339.26	2622.98
6×10^{16}	1.05082	1.16826	3361.58	3755.95
7×10^{16}	1.17923	1.30831	3361.58	3755.95
9×10^{16}	1.60905	1.78016	3053.61	3463.79
1×10^{17}	1.89208	2.09161	2326.84	2589.68

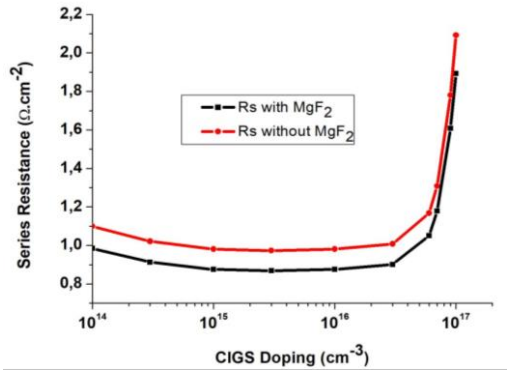

Figure 10. *Apparent series resistance Rs = f(N_A), with and without MgF_2.*

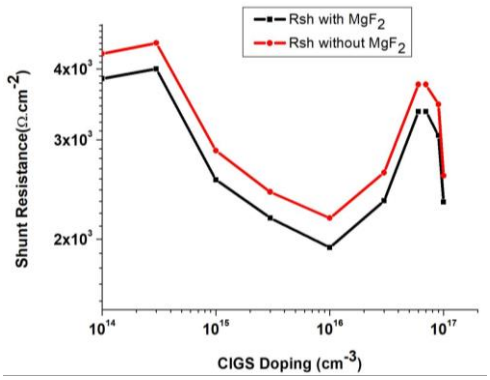

Figure 11. *Apparent shunt resistance Rsh = f(N_A), with and without MgF_2.*

The FF trend identified above motivates a closer look at the apparent parasitic resistances extracted from the same J-V characteristics. Their evolution (Table 8) offers a useful reading of the non-monotonic FF response: at low absorber doping, the relatively high Rs (≈ 1.0-1.1 Ω·cm^2) is consistent with a still-limited electrical transport; increasing N_A initially lowers this apparent resistive limitation, Rs reaching a minimum ≈ 0.87 Ω·cm^2 between 1×10^{15} and 3×10^{15} cm^{-3}, which contributes to the concurrent rise in FF. Beyond the intermediate doping regime, however, Rs climbs markedly, up to 1.89-2.09 Ω·cm^2 at 1×10^{17} cm^{-3}, and this rise tracks the FF degradation closely enough to suggest that the benefit of increased doping has, by that point, been outweighed by additional resistive losses. Rsh follows a more intricate, non-monotonic path: a minimum around 1×10^{16} cm^{-3}, a local maximum around 6-7×10^{16} cm^{-3}, and a further fall at very high doping.

The increase in apparent Rs at high N^A should not be interpreted as an increase in the bulk resistivity of the p-type CIGS absorber. Because Rs is obtained here from the differential slope of the J-V characteristic near Voc, its evolution incorporates the combined influence of junction transport, recombination-induced J-V deformation, and operating-point-dependent differential resistance. It therefore cannot be directly equated with $\rho = (qp\mu_p)^{-1}$.

The relationship between FF and apparent Rs is quantified from the ten simulated doping points considered in this study (Figure 12): the linear correlation coefficient between FF and Rs (with MgF_2) is r ≈ −0.99 across the whole doping range, and r ≈ −0.999 restricted to $N_A > 3\times10^{16}$ cm^{-3}, the region where FF collapses.

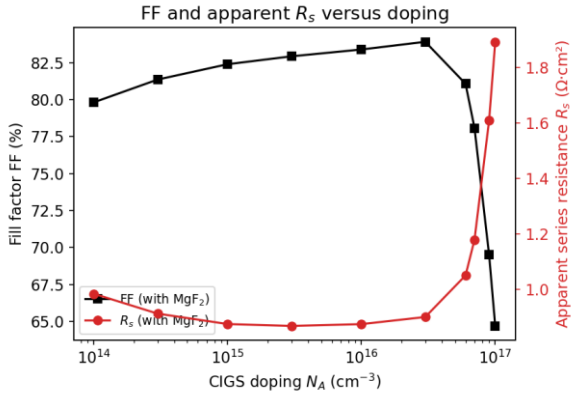

Figure 12. *Fill factor and apparent series resistance versus doping (with MgF_2): the FF drop beyond 3×10^{16} cm^{-3} coincides with the sharp rise in Rs.*

This near-perfect anticorrelation in the collapse region is a quantitative diagnostic of the simultaneous evolution of FF and the apparent differential resistance at high doping. The FF-Rsh correlation is weak across the full range (r ≈ −0.01) but becomes strongly positive (r ≈ +0.91) when restricted to $N_A > 3\times10^{16}$ cm^{-3}, indicating that Rs and Rsh evolve in a coupled rather than independent fashion in that specific region.

It is worth stressing that a statistical correlation between FF and Rs, however strong, is not proof of microscopic causality. This is compounded by the fact that FF and the apparent Rs are both derived from the same simulated J-V curve, so part of their strong association may reflect this shared mathematical origin rather than two fully independent physical observables. Attributing the rise in Rs to intensifying Auger recombination remains a plausible physical interpretation, supported by the well-known cubic dependence of the Auger rate on majority-carrier concentration [22] and by similar observations in other simulation-optimized CIGS architectures, where Auger recombination has been explicitly identified as the factor limiting FF at high acceptor concentration [23]. However, the present simulations do not quantitatively separate the SRH, Auger, and radiative rates, so this interpretation must be stated cautiously: the simultaneous rise in Rs and the FF degradation are consistent with, but do not quantitatively establish, a growing contribution from recombination mechanisms under high-injection conditions.

The non-monotonic Rsh behavior should likewise be interpreted cautiously. Rather than reflecting a simple reduction in parallel leakage paths, this pattern may result from the combined influence of junction electrostatics, interface-state occupancy, and carrier transport.

3.5. Conversion Efficiency: Separating the Electrical and Optical Contributions

Efficiency shows a clear simulated maximum at $N_A = 3\times10^{16}$ cm^{-3} (23.65% with MgF_2, 20.99% without, Table 6, Figure 8). Under the parameter set and assumptions adopted in the present TCAD model, this 23.65% figure should be read as a numerical design prediction rather than as an experimentally demonstrated efficiency; the point of interest is not the absolute value itself but the mechanism that produces it. This optimum coincides with the FF maximum, and hence with the region where Rs is near its local minimum and Rsh near its second local maximum (Section 3.4): since Voc rises and Jsc falls monotonically across the whole studied range, the position of the efficiency optimum therefore coincides primarily with the non-monotonic evolution of FF and with the associated changes in the apparent (Rs, Rsh) diagnostic pair.

The relative efficiency gain from MgF_2 (≈ 12.3-12.8% depending on doping, Table 9) closely tracks the gain observed on Jsc alone (12.16%) and greatly exceeds the negligible gains on Voc and FF. This follows directly from η = Jsc·Voc·FF/Pin: within this model, since MgF_2 affects essentially only Jsc, its effect carries through to the overall efficiency in a nearly proportional way: within the assumptions of the present TCAD model, MgF_2 behaves essentially as an optical element and does not introduce any substantial change to the junction's electrical behavior.

Table 9. *Contribution of MgF_2 to the photovoltaic parameters: average relative gain across the investigated doping range, derived from Tables 3–6.*

Parameter	Average relative gain	Range (min-max)
Jsc	+12.16%	12.16%-12.16%
Voc	+0.42%	0.37%-0.55%
FF	−0.05% (not significant)	−0.28%-+0.07%
η	+12.58%	12.29%-12.83%

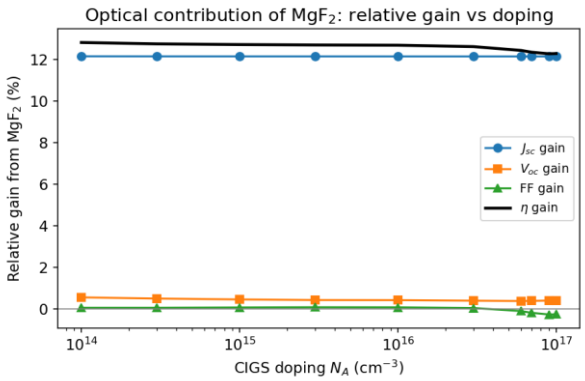

Figure 13. *Relative gain brought by MgF_2 to Jsc, Voc, FF, and η, versus doping: the gain on Jsc and η is nearly constant, confirming the predominantly optical character of MgF_2 in this model.*

3.6. Apparent Differences in Rs and Rsh Between the Two Configurations

Across the whole doping range, Rs is consistently lower with MgF_2 than without it (a difference of 0.02 to 0.20 Ω·cm2 depending on the operating point, Table 8), and Rsh is consistently higher without MgF_2. Since MgF_2 is represented in the present model primarily through its optical function and does not modify the heterojunction band alignment, this difference does not reflect any real change in the device's electrical properties: because Rs and Rsh are local slopes evaluated near Voc and Jsc respectively [14], the vertical shift of the J-V curve caused by the Jsc gain (Section 3.2) slightly shifts the operating point around which the slope is evaluated. The size of this apparent effect (a few percent) remains far smaller than the Rs jump and Rsh drop caused by doping beyond 6×10^{16} cm^{-3} (Section 3.4), which explains why the effect of MgF_2 on FF itself stays negligible despite these visible differences in the apparent Rs and Rsh.

3.7. A Map of Doping Regimes

Bringing together the results of Sections 3.2-3.5, the behavior of the CIGS/In_2S_3 cell across the studied doping range can be summarized in three qualitative regimes, derived from the photovoltaic and apparent-resistance trends reported in Tables 3-6 and 8. Each regime reflects a different balance between the beneficial electrostatic effect of doping and the detrimental transport-related losses that eventually offset it:

1) *Regime I, low doping (10^{14}-10^{15} cm^{-3}):* low Voc, relatively high Rs, collection still limited by an insufficient junction potential; FF and efficiency below 90% of their maximum value.
2) *Regime II, favorable window (≈10^{16}-6×10^{16} cm^{-3}):* Rs near its local minimum, Voc still rising, FF at its peak (≥ 96% of FFmax); efficiency ≥ 95% of the maximum across this whole window, with a nominal optimum at 3×10^{16} cm^{-3}.
3) *Regime III, high doping (> 6×10^{16} cm^{-3}):* Voc keeps rising and Jsc keeps falling, but Rs rises sharply (FF-Rs anticorrelation ≈ −0.999) and Rsh falls back; the fill factor deteriorates sharply and closely tracks the efficiency decline, despite Voc's continued growth.

Table 10. *Physical interpretation of the three doping regimes, built from Tables 3 to 6 and 8.*

Doping regime	Voc	Jsc	FF	Rs (apparent)	Interpretation
Low N_A (10^{14} -10^{15} cm^{-3})	Low	High	Limited	Relatively high	Transport/electrostatic limitation
Intermediate N_A (≈10^{16}-6×10^{16} cm^{-3})	Improved	Moderate	Maximum	Favorable (near minimum)	Optimum electrical balance
High N_A (> 6×10^{16} cm^{-3})	High	Reduced	Degraded	Sharply increased	Growing electrical (resistive) losses

This three-regime picture explains why an optimum exists despite Voc's continuous growth, and why the fill factor rather than Voc or Jsc marks the transition between the favorable and unfavorable doping regimes: the optimum is entirely explained by the non-monotonic behavior of FF, which is itself statistically tied to the joint evolution of Rs and Rsh rather than to Voc or Jsc taken separately. In other words, the optimum doping level does not correspond to a single dominant mechanism but to the point where beneficial and detrimental competing mechanisms are best balanced.

3.8. Comparison with Related Work and Interface Considerations

The team's earlier study on In_2S_3 donor doping N_D, using the same diagnostic pair (Rs, Rsh) [15], offers a mirror-image reading of the heterojunction: on the buffer side, increasing N_D first improves transport and lowers Rs, before excessive doping degrades Voc through enhanced recombination; on the absorber side, the present study shows a partly reversed picture: Voc keeps benefiting continuously from higher N_A, but the high-doping regime is characterized by a pronounced FF deterioration accompanied by a sharp increase in apparent Rs, despite the continued increase in Voc. This complementarity suggests that a joint design map $\eta = f(N_A, N_D)$ would be a natural extension, though it would require new simulations sweeping both parameters at once; it is therefore mentioned as a future direction (Section 3.10) rather than presented as a result of this work.

The model used here also represents the In_2S_3/CIGS interface with a single defect density Dit and a fixed band alignment ($\Delta Ec \approx +0.3$ eV, Section 2.2). Recent atomic-scale observations of sputtered In_2S_3/CIGSe interfaces show that this interface can develop an ordered-vacancy compound whose thickness depends on deposition conditions, with direct consequences for Voc [10]. This real structural complexity, not captured by the single-Dit model used here, is an additional factor, unquantified in this work, that could shift the exact position of the doping window identified in Section 3.3.

3.9. Optical Contribution of the MgF_2 Antireflection Layer

The MgF_2 antireflection layer follows a single-layer quarter-wave design, for which destructive interference minimizes reflectance when the layer thickness satisfies $d = \lambda/(4n)$. With a refractive index $n = 1.38$, the 105 nm thickness used in this simulation corresponds to a target wavelength $\lambda \approx 579.6$ nm $\approx$ 580 nm, close to the peak spectral irradiance of the AM1.5G solar spectrum. This value falls within the 100–110 nm range reported in the literature for single-layer MgF_2 coatings on CIGS solar cells [24, 25]. Comparing the two simulated architectures, with and without MgF_2, effectively provides a loss-separation experiment: since every other layer and parameter is held fixed, any difference in performance between the two configurations can be attributed to the optical role of the antireflection coating rather than to a change in the cell's electrical operating regime. The relatively large improvement in Jsc, together with the comparatively small changes in Voc and FF (Sections 3.2-3.4), indicates that the performance enhancement is predominantly associated with optical coupling. Within the assumptions of the present TCAD model, the MgF_2 layer therefore behaves as a predominantly optical element. This conclusion should be understood as a property of the model rather than an intrinsic statement about the MgF_2 material itself: a real MgF_2 layer could in principle introduce fixed charges, interface effects, or a thickness-dependent spectral reflectance, none of which is represented in the present simulation, where only the thickness and refractive index of MgF_2 enter the optical calculation of carrier generation. Recent work on antireflection coatings for CIGS cells confirms that the current gain from MgF_2 depends on its thickness and can be further improved with double-layer antireflection designs, adding a few extra percent of relative gain over a single layer [26]; the present study varies neither the thickness nor the structure of the MgF_2 layer, which is explicitly noted as a limitation and a future direction below. Taken together, the results of this section suggest that absorber doping and antireflection engineering should not be regarded as equivalent optimization levers: the former primarily reshapes the electrical balance of the heterojunction, whereas the latter acts predominantly on the optical input available to the device.

3.10. Limitations and Future Research Directions

The present TCAD model involves several assumptions that should be considered when interpreting the results. First, the CIGS absorber acceptor concentration is assumed to be spatially uniform, whereas experimentally fabricated absorbers may exhibit non-uniform doping profiles. Second, the In_2S_3/CIGS interface is represented by a single constant interface defect density, which does not account for the possible energy distribution and spatial variation of interface states. Third, the CIGS band gap is kept fixed throughout the absorber, without Ga/In grading. Fourth, the series and shunt resistances discussed in this work are apparent differential quantities extracted from the local slopes of the simulated J–V characteristics and should therefore not be interpreted as direct measurements of intrinsic bulk or contact resistances. Fifth, the predicted device performance has not been experimentally benchmarked against a reference CIGS/In_2S_3 solar cell. Finally, the MgF_2 thickness is fixed and the simulations are restricted to standard AM1.5G illumination at 300 K.

Several extensions emerge naturally from the present results. Future investigations could examine the effect of non-uniform absorber doping and Ga/In band-gap grading, perform a joint optimization of the CIGS acceptor concentration

and In_2S_3 donor concentration, evaluate the influence of MgF_2 thickness and multilayer antireflection designs, and analyze the temperature dependence of the identified doping regimes. Additional spatially resolved TCAD analyses, including carrier-density profiles, electric-field distributions, space-charge-region width, doping-dependent band diagrams, and separate recombination-rate contributions, would also help clarify the microscopic mechanisms underlying the high-doping degradation regime.

4. Conclusions

The core scientific message can be summarized as follows: absorber doping and antireflection engineering act through fundamentally different loss channels. Doping governs the electrical balance between junction electrostatics, carrier transport, and apparent resistive losses, while MgF_2 mainly reduces front-surface optical losses, with an effect that is nearly independent of the doping regime across the studied range.

The present study provides a coupled analysis of the electrical and optical loss mechanisms governing the performance of CIGS/In_2S_3 solar cells. Absorber doping should not be presented merely as a parameter to be optimized at a single point: it defines a trade-off window among junction potential, carrier collection, and apparent resistive losses, with a nominal optimum at $N_A = 3\times10^{16}$ cm^{-3} but a favorable plateau between 1×10^{16} and 6×10^{16} cm^{-3}. This emphasis on a doping window rather than a single optimum is also relevant in the broader context of experimentally induced modifications of CIGS absorber properties, including alkali incorporation, for which recent studies have highlighted the complex interplay between Na doping, defect-related mechanisms, and photovoltaic behavior [27]. The fill-factor collapse beyond this plateau is statistically tied, almost perfectly ($r \approx -0.999$), to the rise in apparent series resistance, although the mechanistic attribution to Auger recombination cannot be regarded as demonstrated by the present data. The MgF_2 layer behaves within the present model as a predominantly optical element, delivering a stable short-circuit current gain of about 12% across the whole studied doping range, and hence an efficiency gain of comparable size, inherited almost entirely from Jsc. Overall, these results indicate that absorber-doping optimization and antireflection-coating engineering are two complementary, non-substitutable levers, electrical and optical respectively, for improving CIGS/In_2S_3 cells, and that tracking them jointly through the apparent parasitic resistances offers a reproducible diagnostic framework for future design studies.

Abbreviations

CIGS	Copper Indium Gallium Selenide (Cu(In,Ga)Se2)
In_2S_3	Indium Sulfide
MgF_2	Magnesium Fluoride
TCO	Transparent Conductive Oxide
TCAD	Technology Computer-Aided Design
SRH	Shockley-Read-Hall (Recombination Model)
AM1.5G	Air Mass 1.5 Global (Standard Solar Spectrum)
EQE	External Quantum Efficiency
OVC	Ordered Vacancy Compound
DOS	Density of States
FF	Fill Factor
Jsc	Short-Circuit Current Density
Voc	Open-Circuit Voltage
Rs	Series Resistance
Rsh	Shunt Resistance

Author Contributions

Moussa Toure: Investigation, Methodology, Writing – original draft

Sidi Mohamed Mohamed-Yahya: Formal Analysis, Validation, Writing – review & editing

Cheick Tidiane Goudiaby: Data curation, Investigation, Software, Writing – original draft

Ahmed Mohamed-Yahya: Validation, Writing – review & editing

Mamadou Lamine Samb: Conceptualization, Supervision, Validation, Writing – review & editing

Data Availability Statement

The data supporting the outcome of this research work has been reported in this manuscript.

Conflicts of Interest

The authors declare no conflicts of interest.

References

[1] Nakamura, M., Yamaguchi, K., Kimoto, Y., Yasaki, Y., Kato, T., Sugimoto, H. Cd-Free Cu(In,Ga)(Se,S)2 Thin-Film Solar Cell with Record Efficiency of 23.35%. IEEE Journal of Photovoltaics (2019), 9(6), 1863-1867. https://doi.org/10.1109/JPHOTOV.2019.2937218

[2] Jackson, P., Wuerz, R., Hariskos, D., Lotter, E., Witte, W., Powalla, M. Effects of heavy alkali elements in Cu(In,Ga)Se2 solar cells with efficiencies up to 22.6%. physica status solidi (RRL) (2016), 10(8), 583-586. https://doi.org/10.1002/pssr.201600199

[3] Amare, A. M., Hwang, I., Jeong, I., Park, J. H., An, J. G., Song, S., Eo, Y.-J., Cho, A., Cho, J.-S., Ahn, S. K., Ahn, S., Gwak, J., Rehan, M., Park, H.-w., Yun, J. H., Kim, K., Shin, D. High-efficiency cadmium-free Cu(In,Ga)Se2 flexible thin-film solar cells on ultra-thin glass as an emerging substrate. Journal of Alloys and Compounds (2025), 1045, 184723.

[4] Powalla, M., Paetel, S., Hariskos, D., Wuerz, R., Kessler, F., Lechner, P., Wischmann, W., Friedlmeier, T. M. Advances in cost-efficient thin-film photovoltaics based on Cu(In,Ga)Se2. Engineering (2017), 3(4), 445-451. https://doi.org/10.1016/J.ENG.2017.04.015

[5] Green, M. A., Dunlop, E. D., Yoshita, M., Kopidakis, N., Bothe, K., Siefer, G., Hao, X. Solar Cell Efficiency Tables (Version 67). Progress in Photovoltaics: Research and Applications (2026). https://doi.org/10.1002/pip.70068

[6] Hariskos, D., Spiering, S., Powalla, M. Buffer layers in Cu(In,Ga)Se2 solar cells and modules. Thin Solid Films (2005), 480-481, 99-109. https://doi.org/10.1016/j.tsf.2004.11.118

[7] Sáez-Araoz, R., Krammer, J., Harndt, S., Köhler, T., Krüger, M., Pistor, P. et al. ILGAR In_2S_3 buffer layers for Cd-free Cu(In,Ga)(S,Se)2 solar cells with certified efficiencies above 16%. Progress in Photovoltaics: Research and Applications (2012), 20, 855-861. https://doi.org/10.1002/pip.2268

[8] Khoshsirat, N., Yunus, N. A. M. Numerical Analysis of In_2S_3 Layer Thickness, Band Gap and Doping Density for Effective Performance of a CIGS Solar Cell Using SCAPS. Journal of Electronic Materials (2016), 45(11), 5721-5727. https://doi.org/10.1007/s11664-016-4744-6

[9] Ashraf, M. A., Alam, I. Numerical simulation of CIGS, CISSe and CZTS-based solar cells with In_2S_3 as buffer layer and Au as back contact using SCAPS 1D. Engineering Research Express (2020), 2(3), 035015. https://doi.org/10.1088/2631-8695/abade6

[10] Cojocaru-Mirédin, O. et al. Ordered Vacancy Compound Formation at the Interface of Cu(In,Ga)Se2 Absorber with Sputtered In_2S_3-Based Buffers: An Atomic-Scale Perspective. Solar RRL (2024). https://doi.org/10.1002/solr.202400574

[11] Gning, Y., Ngom, A., Touré, M., Sam, M., Namena, E., Samb, M. L. Influence de la bande interdite optique et de l'affinité électronique du ZnSe sur les performances des cellules solaires CIGS. International Journal of Innovation and Applied Studies (2026), 48(1), 92-108.

[12] Asaduzzaman, M., Hasan, M., Bahar, A. N. An investigation into the effects of band gap and doping concentration on Cu(In,Ga)Se2 solar cell efficiency. SpringerPlus (2016), 5, 578. https://doi.org/10.1186/s40064-016-2256-8

[13] Agoundedemba, M., Baneto, M., Nyenge, R., Musila, N., Touré, K. J. N. Improving FTO/ZnO/In_2S_3/CuInS2/Mo solar cell efficiency by optimizing thickness and carrier concentrations of ZnO, In_2S_3 and CuInS2 thin films using Silvaco-Atlas software. International Journal of Renewable Energy Development (2023), 12(6), 1131-1140.

[14] Hegedus, S. S., Shafarman, W. N. Thin-film solar cells: device measurements and analysis. Progress in Photovoltaics: Research and Applications (2004), 12(2-3), 155-176. https://doi.org/10.1002/pip.518

[15] Gning, Y., Biagui, M., Touré, M., Touré, A., Samb, M. L. Donor-Doping Optimization of In_2S_3 Buffer Layers in CIGS Solar Cells: A TCAD Diagnostic of Transport-Recombination-Leakage Competition via Rs and Rsh. Journal of Materials Science and Chemical Engineering (2026), 14(4), 1-19.

[16] Silvaco Inc. ATLAS User's Manual: Device Simulation Software. Silvaco International, Santa Clara, CA, USA (2016).

[17] Rolles, M. Étude théorique de la faisabilité des LED à base de ZnGeN2. Doctoral thesis, Université de Lorraine, Nancy, France, pp. 63-65 (2018).

[18] Sze, S. M., Ng, K. K. Physics of Semiconductor Devices, 3rd edition. Wiley-Interscience, Hoboken, NJ, USA (2007).

[19] Rau, U., Schmidt, M. Electronic properties of ZnO/CdS/Cu(In,Ga)Se2 solar cells — aspects of heterojunction formation. Thin Solid Films (2001), 387(1-2), 141-146.

[20] Rau, U., Paetel, S., Werner, J. H. Band alignment and interface recombination in CIGS-based heterojunction solar cells. Physical Review B (2003), 67, 045203.

[21] Carron, R., Avancini, E., Feurer, T., Bissig, B., Losio, P. A., Figi, R. et al. Refractive indices of layers and optical simulations of Cu(In,Ga)Se2 solar cells. Science and Technology of Advanced Materials (2018), 19(1), 396-410. https://doi.org/10.1080/14686996.2018.1458579

[22] Kerr, M. J., Cuevas, A. General parameterization of Auger recombination in crystalline silicon. Journal of Applied Physics (2002), 91(4), 2473-2480. https://doi.org/10.1063/1.1432476

[23] Rahman, M. F., Chowdhury, M., Marasamy, L., Mohammed, M. K. A., Haque, M. D., Al Ahmed, S. R., Irfan, A., Chaudhry, A. R., Goumri-Said, S. Improving the efficiency of a CIGS solar cell to above 31% with $Sb2S_3$ as a new BSF: a numerical simulation approach by SCAPS-1D. RSC Advances (2024), 14, 1924-1938. https://doi.org/10.1039/d3ra07893k

[24] Rezaei, N., Isabella, O., Vroon, Z., Zeman, M. Optical optimization of a multi-layer wideband anti-reflection coating using porous MgF_2 for sub-micron-thick CIGS solar cells. Solar Energy (2019), 177, 59-67. https://doi.org/10.1016/j.solener.2018.11.015

[25] Ahmad, F., Civiletti, B. J., Monk, P. B., Lakhtakia, A. Efficiency enhancement of ultrathin CIGS solar cells by optimal bandgap grading. Part II: finite-difference algorithm and double-layer antireflection coatings. Applied Optics (2022), 61(33), 10049-10061. https://doi.org/10.1364/AO.474920

[26] Ahmad, F., Civiletti, B. J., Monk, P. B., Lakhtakia, A. Double-Layer Antireflection Coatings for CIGS Thin-Film Solar Cells. Proceedings of SPIE (2023), 12477, 124770E. https://doi.org/10.1117/12.2645881

[27] Zi, G., Li, D., Yuan, M., Xin, W., Hong, R. Study on the Mechanisms of Na Doping in CIGSe Solar Cells via a Solution-Based Method. ACS Applied Energy Materials (2025), 8(1), 412-420. https://doi.org/10.1021/acsaem.4c02518